


Investigating the Poisson Ratio of 3D Printed Concrete

Jacques Kruger *  and Jean-Pierré van der Westhuizen

Department of Civil Engineering, Stellenbosch University, Stellenbosch 7600, South Africa

* Correspondence: pjkruger@sun.ac.za

Abstract: Poisson's ratio, defining the lateral to longitudinal strain of a material under uniaxial load, is an extensively used material property in engineering analysis and design. For conventionally cast concrete, an isotropic static Poisson ratio typically ranges between 0.15 to 0.25. However, no ratio has been established for 3D printed concrete, and is currently widely assumed to be 0.2 and isotropic in computational modelling applications. This layer-wise additive manufacturing technology is notorious for yielding orthotropic mechanical properties due to the presence of weak interlayer regions at the structural level and elongated oblate voids at the material level. This study therefore aims to characterise the static Poisson ratio of printed concrete. Specimens were prepared from a printed element and uniaxially tested both parallel and perpendicular to the printing direction. Digital image correlation technology was employed to facilitate the capturing of specimen strains, followed by micro-computed tomography scans to determine void topography. The results indicate larger Poisson ratios apply for 3D printed concrete compared to its cast counterpart; up to 17 and 33% increases were obtained when printed specimens were tested perpendicular and parallel to the printing direction, respectively. This orthotropic behaviour is ascribed to the oblate voids present in the printed specimens.

Keywords: 3D printed concrete; Poisson's ratio; experimental testing; digital image correlation; micro-computed tomography



Citation: Kruger, J.; van der Westhuizen, J.-P. Investigating the Poisson Ratio of 3D Printed Concrete. *Appl. Sci.* **2023**, *13*, 3225. <https://doi.org/10.3390/app13053225>

Academic Editors: Laurent Daudeville and Kang Su Kim

Received: 27 January 2023

Revised: 14 February 2023

Accepted: 1 March 2023

Published: 2 March 2023



Copyright: © 2023 by the authors. Licensee MDPI, Basel, Switzerland. This article is an open access article distributed under the terms and conditions of the Creative Commons Attribution (CC BY) license (<https://creativecommons.org/licenses/by/4.0/>).

1. Introduction

Poisson's ratio (ν) is a unitless material property defined as the measure of an unconfined material's lateral strain (ϵ_{lat}) relative to its longitudinal strain (ϵ_{long}) under uniaxial loading, expressed as $\nu = -(\epsilon_{lat}/\epsilon_{long})$, where contraction is taken as negative and elongation as positive. Typically, Poisson's ratio varies between 0 and 0.5 for most materials, where the former refers to a material that experiences a significant volume change under axial load (e.g., cork material), and the latter an incompressible material that experiences no volume change under axial load (e.g., rubber materials) [1]. Negative Poisson values are also possible, referred to as auxetic materials, where tri-contraction along Cartesian axes arises from uniaxial compression [2,3]. The use of Poisson's ratio in engineering and mechanics is widespread; most notably, it influences the stress distribution and concentrations within a material [4]. Referring specifically to structural mechanics, Poisson's ratio forms an integral part in defining constitutive laws describing stress–strain relationships as well as the elastic–shear moduli relationship. Composite column performance has also been demonstrated to be influenced by the Poisson effect [5].

Although Poisson's ratio of conventionally cast concrete is well established in the literature, typically ranging between 0.15–0.25 [6], no research data are currently available in the literature on the Poisson ratio of 3D printed concrete. The authors hypothesise that, unlike conventionally cast concrete that is typically homogenous and isotropic, the static Poisson ratio of 3D printed concrete is anisotropic. Kruger, du Plessis and van Zijl [7] investigated the microporosity of 3D printed concrete via micro-computed tomography and found that its void topology differs from that seen in conventionally cast concrete. Compared with dominantly spherical shaped voids in cast concrete, intralayer voids in

3D printed specimens are elongated, with their largest dimension in the printed direction followed by the transverse direction and the smallest in the vertical direction. As a premise for a follow-up study [8], it was demonstrated that (i) 3D printed concrete exhibits reduced mechanical performance compared to its cast equivalent, and (ii) orthotropic compressive strengths are prevalent in 3D printed concrete. This orthotropic mechanical nature of 3D printed concrete is widely reported in the literature [9–15].

The theoretical grounding of this study's hypothesis lies in the stress concentrations that develop around micro-voids in a continuum under uniaxial loading. A study by Davis et al. [16] demonstrated that as a void becomes more oblate (as was shown in [7] for 3D printed concrete), the compressive stress developed at its extreme lateral sides/tips increases under uniaxial loading. This localized, concentrated compressive stress reduces as a void becomes more prolate; hence the difference between the (relatively constant) tensile stress developed at poles and the compressive stress developed at sides reduces. Following hereon, it can be deduced that the magnitude of strain experienced in a porous material is influenced by its void topology, where predominantly oblate or prolate voids could lead to orthotropy.

Due to the current lack of information on the Poisson ratio for 3D printed concrete, several studies conducted on finite element modelling of printed concrete have adopted typical isotropic Poisson values of conventionally cast concrete, i.e., 0.2 [17–22] and 0.21 [23]. Thus, no account was made for possible anisotropy in this regard. Similar to fresh state buildability modelling, comprising plastic yielding and elastic buckling failure mechanisms [24], the Poisson value for fresh printable concrete was assumed to be 0.3 [25–27], mainly adopted from the early experimental work conducted by Wolfs, Bos and Salet [28,29]. In another study by Moïni et al. [30], the fresh state Poisson value was assumed to be 0.5, which, as mentioned earlier, is considered incompressible. The saturation state of fresh concrete, i.e., the amount of free water available to fill pores, influences the Poisson ratio; therefore, fresh concrete can possess Poisson values ranging up to that of water, namely 0.5 [31]. The state of hydration thus influences fresh concrete's Poisson ratio, resulting in a transient property that only stabilises after roughly 28 days' curing time [32]. The modelling of accelerated fresh concrete, typically using 2K 3D printing systems [33], therefore requires rigorous exploration toward an accurate and representative Poisson ratio expression. The shape retention performance of extruded concrete has also been shown to be influenced by its Poisson ratio [34].

It is with this background that this study endeavours to perform a preliminary investigation into the hardened-state Poisson ratio of extrusion-based 3D printed concrete. Although the subject is critically important, this study does not investigate the Poisson ratio of fresh-state printable concrete. The static Poisson ratio was determined for a 3D printable cementitious material in two distinct orientations (O1: perpendicular to the print path, OIII: parallel to the print path [35]), as well as for its cast equivalent. ASTM C469-02 [36] was used as a testing guideline and amended for the sample size obtained from 3D printing. Digital image correlation (DIC) technology was employed to accurately record deformation of strategically placed target markers, from which data the Poisson values were derived. In order to ascertain hypothesis significance, statistical method ANOVA (analysis of variance) was applied. Lastly, the specimens' microporosities were visualised via micro-computed tomography, which confirmed that the typical oblate-shaped voids in printed concrete were present in this study's specimens.

2. Materials and Methods

2.1. 3D Printing

The standard high-performance 3D printable cementitious mixture typically employed at Stellenbosch University [37] was used for this study, with constituents and quantities given in Table 1. This mixture possesses a 28-day compressive strength and Young's modulus of approximately 70 MPa and 30 GPa, respectively. Initially, all binder materials were weighed and sieved through a 1 mm sieve to eliminate any clumps that may have

formed. Thereafter, the fine aggregate was weighed and added to a 50 L 2-blade pan mixer, together with the binder material, and mixed until homogeneously distributed. Potable tap water was then added and mixed for 2 min. Finally, the superplasticiser admixture was added to obtain the required workability for printing.

Table 1. Three-dimensional printing cementitious material used for this study.

Constituent	Description	kg
Cement	PPC SureTech 52.5 N	579
Fly ash	DuraPozz Class F	165
Silica fume	Chryso DSF	83
Fine aggregate	Malmesbury 4.75 mm MPS ¹	1167
Water	Potable Tap Water	261
Superplasticiser	Chryso Premia 310	5.75

¹ Maximum particle size.

The 40 L batch of mixed material was transferred to the rotor-stator pump's hopper, and the system was bled to ensure proper extrudability. A 1 m³ gantry-type 3D concrete printer was used to print two arbitrary objects from which the specimens were obtained for testing. These objects all possessed double-skin wall elements of 200 mm height, as depicted in Figure 1. A rectangular nozzle was employed, of which the cross-sectional opening measured 50 mm wide and 20 mm high, also equal to the filament layer height and deposition height or nozzle standoff distance. A print speed of 60 mm/s was used, resulting in a pass time of roughly 30 s. The printing was conducted in a climate-controlled room, with temperature 23 ± 2 °C and relative humidity $65 \pm 5\%$. These wall elements were left to cure in the climate-controlled room for 27 days, whereafter specimen extraction and preparation followed. We also cast $100 \times 100 \times 100$ mm cubes using the 3D printable material, which were used to extract the cast specimens for comparison purposes. Two casting methods were followed, namely (i) material pumped through a nozzle to fill the plastic cube mould and (ii) material scooped from the pan mixer to fill the plastic cube mould. The cast specimens were also cured in a climate-controlled room for a period of 27 days.

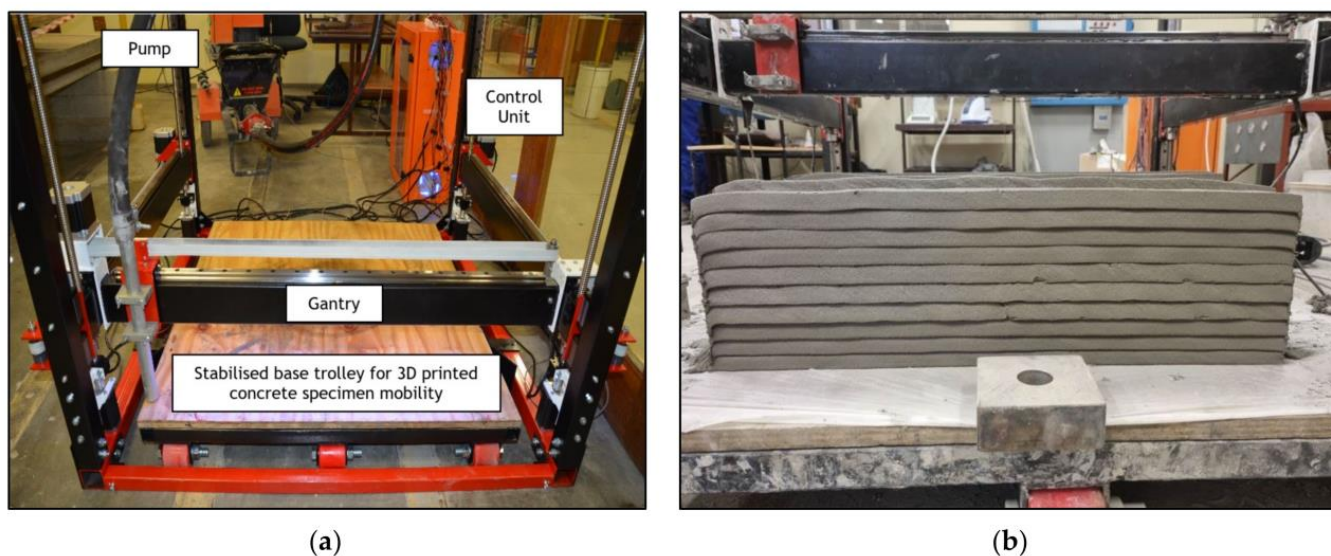


Figure 1. (a) Three-dimensional concrete printer coupled with a batch mix rotor-stator pump, as used in this research; (b) two double-skin free-standing 3D printed wall elements from which specimens were extracted for testing.

2.2. Specimen Preparation

Specimens were extracted from the printed wall elements and cast cubes by means of core drilling, coupled with a diamond tip core bit, as specified by ASTM C469-02 [36]. This norm specifies that cores should have a height-to-diameter ratio of at 1.5 or higher. The authors opted for cylindrical specimens of height 60 mm and diameter 30 mm, yielding a height-to-diameter ratio of 2. Specimens were extracted from the printed elements in two distinct orientations, namely OI, perpendicular to the print path, and OIII, parallel to the print path [35]. Thus, voids in the OI specimens were oblate, whereas voids in OIII were prolate, relative to applied uniaxial compression. Cores of 200 mm length were only taken from within a single filament skin as to avoid having doubly orientated interlayers in the test specimen. The cores were then saw cut down to 60 mm in length, and the ends surface grinded to ensure planeness. Figure 2 depicts the specimen extraction positions on the printed elements.

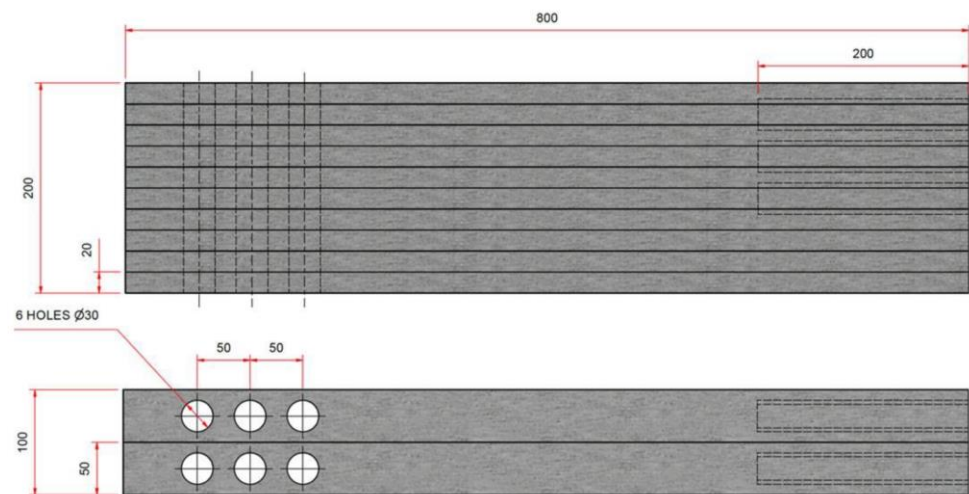


Figure 2. Positions and orientations of cored specimens from the printed elements. OI specimens are shown on the left and OIII on the right. The top image depicts a front elevation view and bottom image plan view. Units in mm.

Figure 3 shows the interlayer orientations for the OI and OIII test specimens. Care was taken to ensure that OI specimens comprise of three filament layers of 20 mm each, thus saw cutting on interlayers for the ends. Similarly, OIII specimens comprised 3 filament layers, with the middle layer centred. Five specimens were prepared for testing.

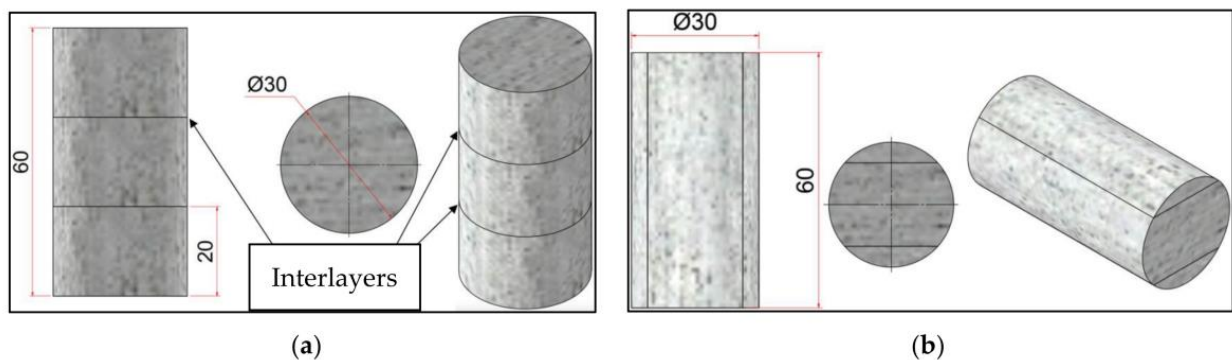


Figure 3. (a) OI test specimen with interlayers horizontal; (b) OIII test specimen with interlayers vertical. Units in mm.

Specimens were also core drilled for micro-computed tomography (μ -CT) scanning. Generally, smaller specimens provide higher resolution; therefore, these specimens were

cut to 20 mm in height at 30 mm diameter, with the interlayer region located in the middle (10 mm height). Four specimens were drilled for this purpose, two in the OI orientation, of which one was extracted from the top half of the printed element designated 3DCPOIT and the other from the bottom half designated 3DCPOIB, and two specimens were extracted from the cast cubes, designated CAST-CM for conventional casting and CAST-3DCP for the extruded concrete. No OIII specimen was prepared for μ -CT scanning, since the void topology would be similar to that of OI, albeit rotated vertically. Figure 4 depicts the specimens prepared for μ -CT scanning.

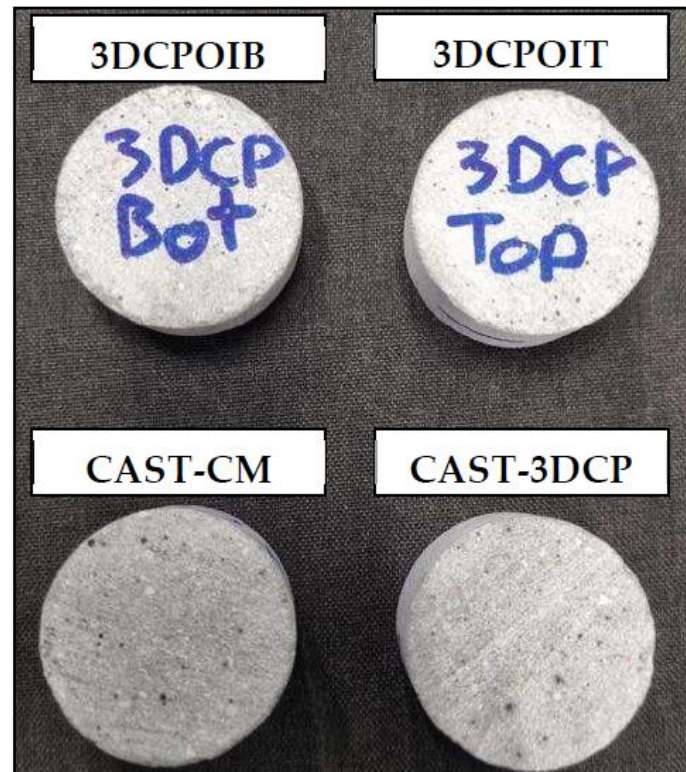


Figure 4. Core-drilled specimens of 20 mm height and 30 mm diameter for μ -CT scanning.

2.3. DIC, Target Marker Design, and Assembly

ASTM C469-02 [36] specifies that either an unbonded extensometer or strain gauges may be used to determine the transverse or lateral strain for Poisson ratio determination. Due to the laboratory not possessing an unbonded extensometer setup, and considering the large number of specimens to test combined with the small surface area for gauge mounting, the authors decided to employ 2D digital image correlation (DIC) technology. This technology, which yields high resolution in concrete applications if correctly set up [38], enables the synchronization of lateral and vertical strain capturing during testing that results in highly accurate Poisson ratios. In this research, a Basler acA2040-55 μ m camera with resolution 2048×1536 pixels was coupled with an Edmund Optics 35 mm/F1.65 lens for image acquisition. The Basler Pylon camera software (V7.2.1) suite facilitated the capturing and data storage process. By utilising the Basler Lens Selector tool, it was determined that the camera must be located at a working distance of 585 mm in order to achieve a field-of-view with dimensions 112 mm wide and 83 mm high, i.e., slightly higher than the test specimen. This configuration yielded a pixel size (resolution) of roughly 50 μ m. An acquisition rate of 1 Hz was chosen.

GOM Correlate software (2021) was used for the analysis of the data [39]. Since only one camera was used, only a 2D analysis could be performed. However, since the test specimens were cylindrical in a 3D space, in-plane aligned target markers were required to provide a 2D reference point at any point of surface contact on the test specimen. These

target markers were identifiable by the software and were used to compute the relative in-plane strain difference over the monochrome image series input. The target markers contained nine differentiable point components that each represented an ellipsoid with major and minor axis lengths of 10 ± 2 pixels, based on the field-of-view dimensions. A summary of the DIC setup information is given in Table 2.

Table 2. Summary of the DIC setup information.

Resolution Pixels	Working Distance mm	Field-of-View mm	Pixel Size μm	Ellipse Major Axis μm	Ellipse Minor Axis μm
2084 × 1536	585	112 × 83	≈50	656	547

The target markers were fixed to the test specimen by using tiny 2 mm thick Perspex blocks, epoxy-glued to the specimen, with a 1 mm hole in the centre through which the target marker's pin fit. This facilitated planeness, i.e., aligned all target markers depth-wise, achieving a consistent distance from the camera. An image of a test specimen with two fixed lateral Perspex blocks is shown in Figure 5.



Figure 5. Test specimen with two lateral Perspex blocks attached for target marker positioning.

Target markers were also used for longitudinal strain capturing. A steel platen was placed below and above the test specimen for the uniaxial compression test. Since a target marker could not be placed directly between the specimen's surface and each platen, the authors decided to fix the target markers on the inside of the steel platens, next to the test specimen. Such positioning would only capture the test specimen's deformation and exclude that of the steel platens. The final test specimen DIC assembly comprised six in-plane target markers. Four target markers were used to capture longitudinal strain, and two markers placed laterally at the specimen's mid-height, where maximum lateral strain would occur. A DIC recorded image of an assembled test specimen is shown in Figure 6.

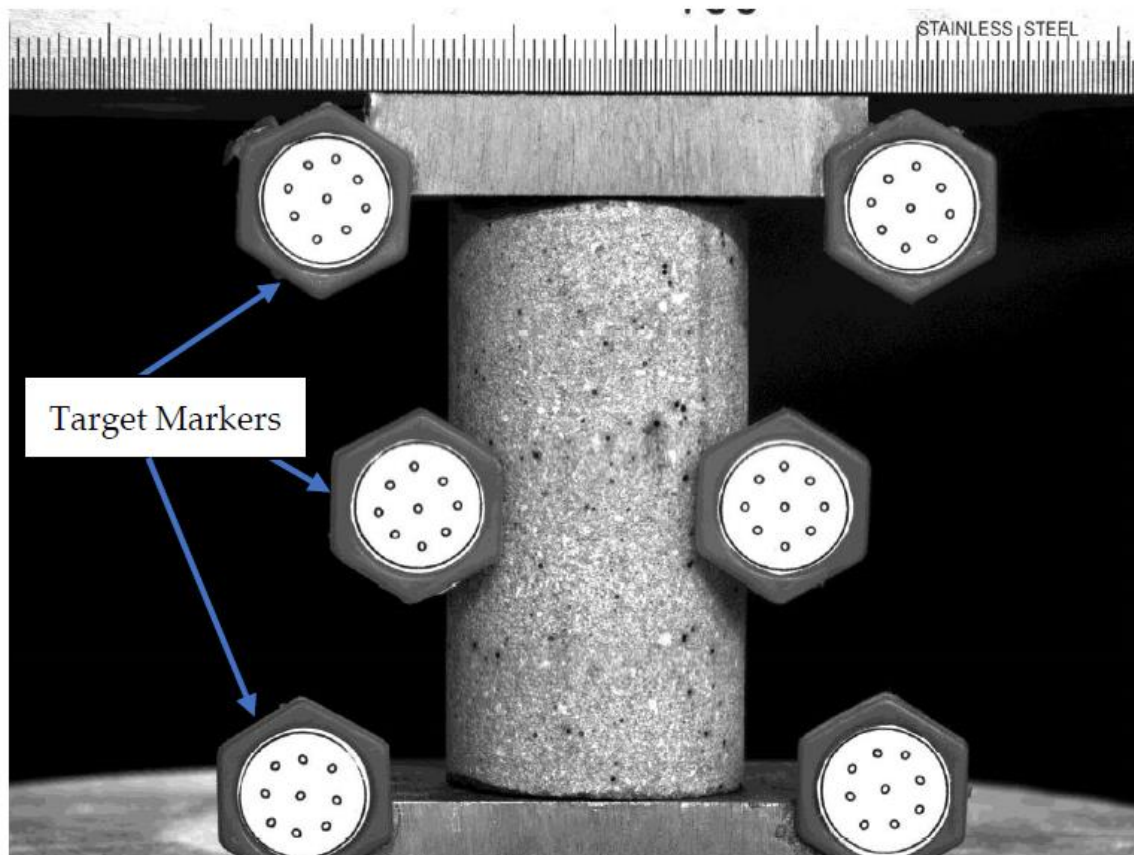


Figure 6. A DIC monochrome image of an assembled test specimen containing six target markers, with nine point-components each. Four target markers (two below top platen and two above bottom platen) track longitudinal strain while two target markers placed laterally at specimen mid-height track lateral strain. A ruler with 10 mm increments is placed above the specimen to calibrate the acquired strains.

2.4. Testing Procedure

ASTM C469-02 [36] prescribes that either a position-controlled head displacement rate of 1.25 mm/min or a stress-controlled rate of 241 ± 34 kPa/s may be employed for a uniaxial compression test. In this research, with specimen diameter of 30 mm, a force-controlled rate of 150 N/s was used, resulting in a stress rate of 212.2 kPa/s, which was in the allowable range. Load was only applied up to 40% of the specimen's ultimate load, here equalling 6 kN. The compressive testing was facilitated by a Zwick Z250 materials testing machine. Three load repetitions were performed per specimen, of which only the last two were used to determine Poisson's ratio. The force readings obtained from the Zwick were synchronised with the strain readings from the DIC by means of timestamps. Poisson's ratio was then determined according to the following equation [36]:

$$\nu = \frac{(\epsilon_{t2} - \epsilon_{t1})}{(\epsilon_2 - 0.00005)} \quad (1)$$

where ν is Poisson's ratio, ϵ_{t2} the lateral strain at mid-height of the specimen produced at 40% of ultimate load, ϵ_{t1} the lateral strain at mid-height of the specimen produced at a stress corresponding to a longitudinal strain of 50 millionths, and ϵ_2 the longitudinal strain produced at 40% of the ultimate load. The Poisson ratio was taken as the average of the last two load repetitions performed per specimen. Five specimens were tested for each configuration.

2.5. Micro-Computed Tomography

Micro-computed tomography (μ -CT) scanning was performed at the Central Analytical Facilities of Stellenbosch University using the General Electric Nanotom S CT scanner and data analysis was performed using Volume Graphics VGSTUDIO MAX 3.4. A voxel size of 22 μm was employed using 120 kV and 90 μA for X-ray generation. The images were captured while the sample was rotated 360° at 2800 images per rotation. The data were de-noised using an adaptive Gauss filter. In addition to providing the total porosity volume fraction, each individual pore space was listed with its volume, surface area, maximum diameter, compactness, projected size in each axis, etc. Compactness (unitless) was defined as the ratio of the volume of the pore over the volume of a perfect sphere fitting around the pore, that is, the circumscribed sphere. Therefore, an ideal spherical pore space has a compactness value of 1. Sphericity was measured similarly, only that the surface area of a void was used and not its volume. Figure 7 depicts the General Electric Nanotom S CT scanner utilised in this research.



Figure 7. The General Electric Nanotom S CT scanner used to determine the porosity characteristics of the 3D printed and cast concrete in this study.

3. Results

3.1. Poisson's Ratio

The results of the Poisson ratio testing are given in Table 3 for the CAST-CM, OI and OIII groups. An average value was determined for each group based on all five specimens tested within the group. It was found that the conventionally cast printable concrete (CAST-CM) had a Poisson ratio of 0.18, which is within the typical range of 0.15–0.25 for hardened cast concrete. The 3D printed specimen tested in OI orientation, i.e., load perpendicular to print direction yielding oblate voids, was found to have a higher ratio of 0.21. Furthermore, the 3D printed specimen tested in OIII orientation, i.e., load parallel to print direction yielding prolate voids, was found to have the highest ratio of all groups at 0.24. Thus, the Poisson ratios of 3D printed concrete in this study are 17% and 33% higher in OI and OIII, respectively, compared to its cast equivalent. The one-way ANOVA performed between all three groups tested, shown in Table 4, yielded a p -value of 0.0047. This value is approximately an order of magnitude less than the significance value of 0.05, thereby confirming the null hypothesis that there is a statistical difference between the means of the three groups.

Table 3. Poisson ratios of CAST-CM, OI and OIII, taken as the average of 5 specimens per configuration.

Specimen Configuration	Specimen Number	Height mm	Diameter mm	δ_{lat} mm	δ_{long} mm	ϵ_{lat} mm/mm	ϵ_{long} mm/mm	ν	ν_{avg}
CAST-CM	1	59.61	29.81	0.01	−0.1	0.000336	−0.001678	0.2	0.18
	2	59.67	29.84	0.01	−0.13	0.000335	−0.002179	0.15	
	3	59.65	29.95	0.01	−0.11	0.000334	−0.001844	0.18	
	4	59.59	29.81	0.01	−0.1	0.000335	−0.001678	0.2	
	5	59.62	29.93	0.01	−0.11	0.00034	−0.001845	0.18	
OI	1	59.01	29.76	0.01	−0.11	0.000336	−0.001864	0.18	0.21
	2	59.04	29.77	0.01	−0.10	0.000336	−0.001609	0.21	
	3	59.00	30.10	0.01	−0.09	0.000332	−0.001441	0.23	
	4	59.03	29.76	0.01	−0.10	0.000336	−0.001660	0.20	
	5	59.03	29.71	0.01	−0.10	0.000337	−0.001643	0.20	
OIII	1	59.95	29.83	0.01	−0.08	0.000335	−0.001334	0.25	0.24
	2	59.95	29.82	0.01	−0.09	0.000335	−0.001501	0.22	
	3	59.93	29.80	0.01	−0.08	0.000336	−0.001335	0.25	
	4	59.95	29.83	0.01	−0.1	0.000335	−0.001668	0.20	
	5	59.95	29.80	0.01	−0.08	0.000336	−0.001335	0.25	

Table 4. One-way ANOVA result of all tested groups.

Groups	Count	Sum	Average	Variance		
Cast-CM	5	0.92	0.18	0.000358		
OI	5	1.03	0.21	0.000321		
OIII	5	1.18	0.24	0.000523		
Source of Variation	SS	df	MS	F	p-value	F crit
Between groups	0.0069	2	0.00347	8.6661	0.0047	3.8853
Within groups	0.0048	12	0.00040			
Total	0.0118	14				

3.2. Porosity, Sphericity and Compactness

The porosity characteristics of all the scanned specimens are given in Table 5. Clearly, the cast specimens, both CAST-CM and CAST-3DPC, have lower porosity than their 3D printed counterparts at 1.61% and 1.84%, respectively. It is further evident that the pumping and extrusion process increases porosity, as CAST-3DCP has a slightly higher porosity than CAST-CM. The highest porosity of 5.67% was obtained for the 3DCPOIB specimen, extracted from the bottom of the printed element, as shown in Figure 2. The specimen extracted from the top of the printed element, 3DCPOIT, has a porosity of 2.65%, less than half of its 3DCPOIB counterpart. It is unknown at this stage what could have led to this discrepancy, but this warrants further investigation. However, since a large fraction of the porosity was located at the interlayer regions, it is clear that air entrapment occurs during the successive deposition (printing) process, resulting in the 3D printed specimens having higher porosity than their cast counterparts. Thus, the material deposition process has a larger influence on porosity than the pumping and extrusion process.

The sphericity and compactness of all the scanned specimens are depicted in Figure 8. Both these measures follow identical patterns. The CAST-CM specimen has the highest sphericity and compactness, i.e., voids in this specimen are the most spherical/rounded, as is expected of conventionally cast concrete. Thereafter follows CAST-3DCP, which indicates that the pumping and extrusion process does have an influence on void topology. The 3D printed specimens have the lowest sphericity and compactness, which indicates that the successive deposition (printing) process also influences void topology, more so than the pumping and extrusion process. Interestingly, the 3DCPOIB specimen has the lowest sphericity and compactness, confirming a spatial variation in porosity and void topology exists over the height of a printed element. The authors postulate that a combination

of overlay compaction [40] and bearing resistance capacity of freshly deposited concrete contribute toward this spatial variation.

Table 5. Porosity characteristics of all specimen groups obtained from μ -CT scanning.

Specimen Characteristics	Unit	CAST-CM	CAST-3DPC	3DPCOIB	3DPCOIT
Voxel	Voxel	19,188,360	21,931,200	59,887,344	35,192,596
Proj. area (yz)	mm ²	960.37	2166.47	3375.27	2873.17
Volume	mm ³	204.31	233.52	637.68	374.73
Proj. area (xz)	mm ²	1015.22	2339.31	3878.10	2771.90
Surface area	mm ²	6028.75	12,937.23	23,833.75	17,764.57
Proj. area (xy)	mm ²	1080.25	2362.37	4502.17	3350.73
Material volume	mm ³	12,495.13	12,425.50	10,599.98	13,780.40
Defect volume	mm ³	204.32	233.52	637.68	374.73
Defect ratio/porosity	%	1.61	1.84	5.67	2.65

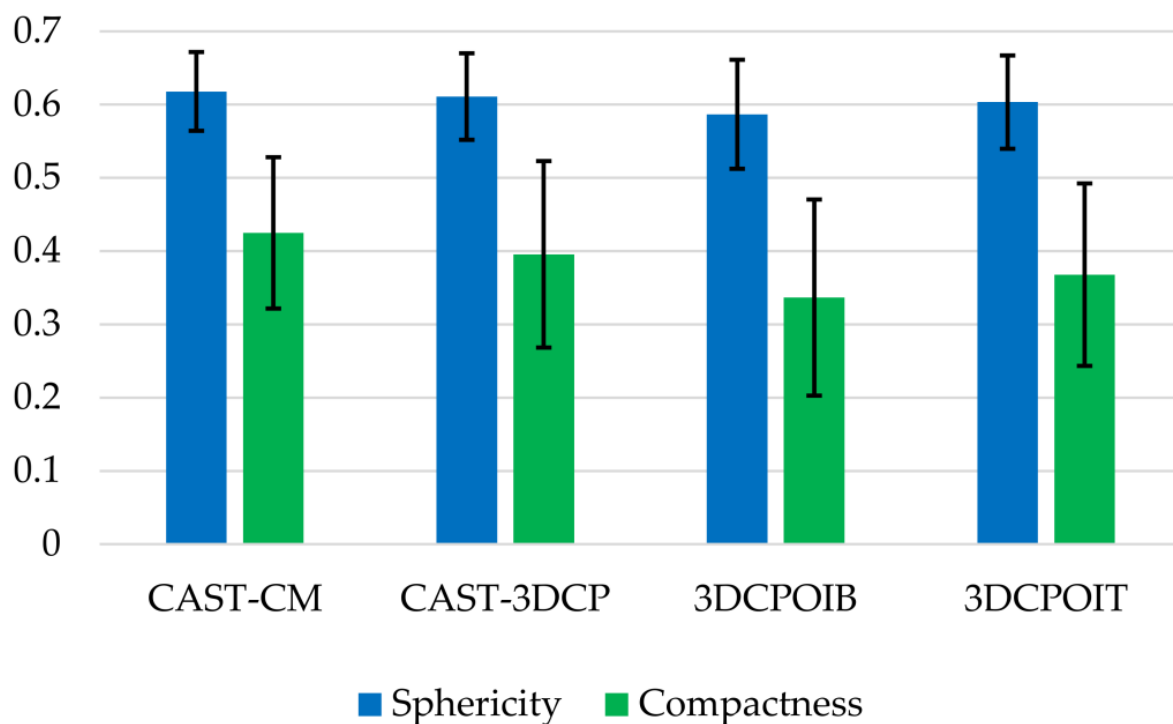


Figure 8. Sphericity and compactness means of all specimen groups obtained from μ -CT scanning. Error bars indicate standard deviation. Values are unitless; however, a value of 1 equals an ideal spherical pore space.

3.3. Void Topology

The results from the μ -CT scans of the four specimen configurations were plotted comparing the void diameter to the void length in each Cartesian direction. The void diameter refers to the largest dimension present in the void, while the void length refers to the longest measurement for each of the x, y and z Cartesian directions. The x-direction denotes the printing direction, y the lateral dimension, and z the vertical dimension or height of the void. Linear regression was applied to the data as a means of distinguishing between averages toward deriving conclusions. These graphs are depicted in Figures 9–12 for all the specimen configurations.

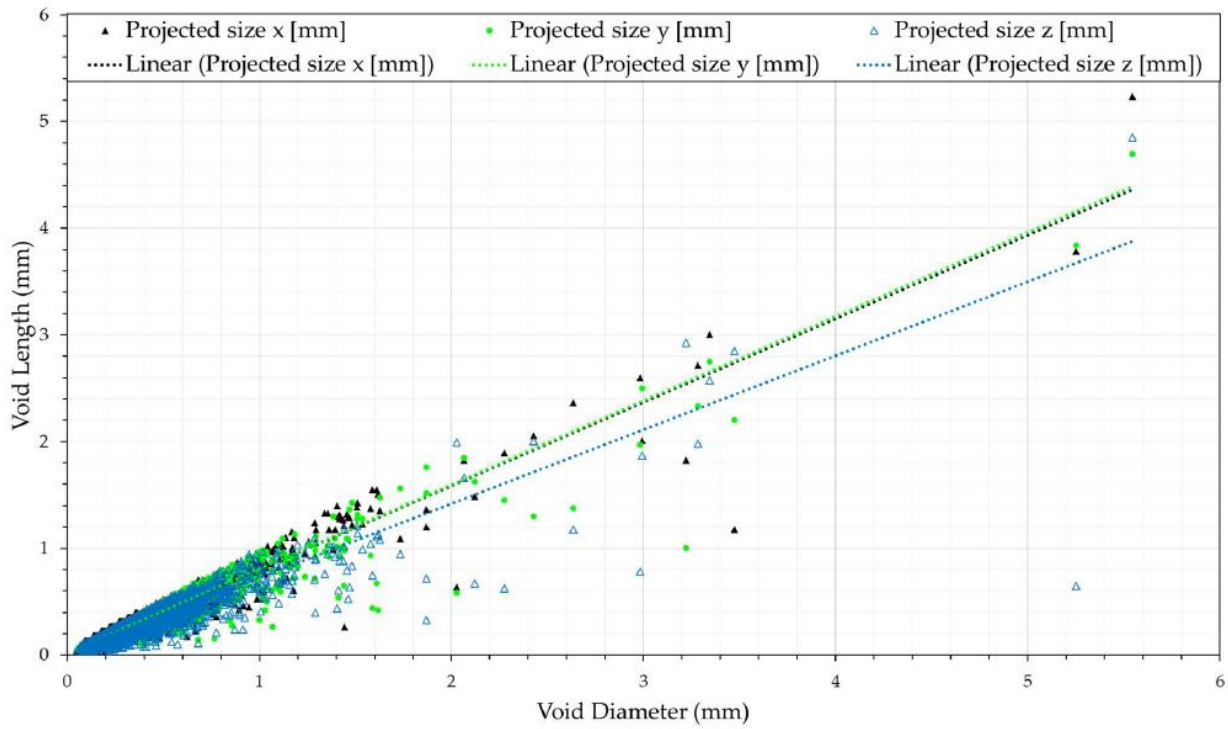


Figure 9. CAST-CM void topology from μ -CT scanning. The coefficients of determination (R^2) for x, y and z linear regression are 0.91, 0.92 and 0.87, respectively.

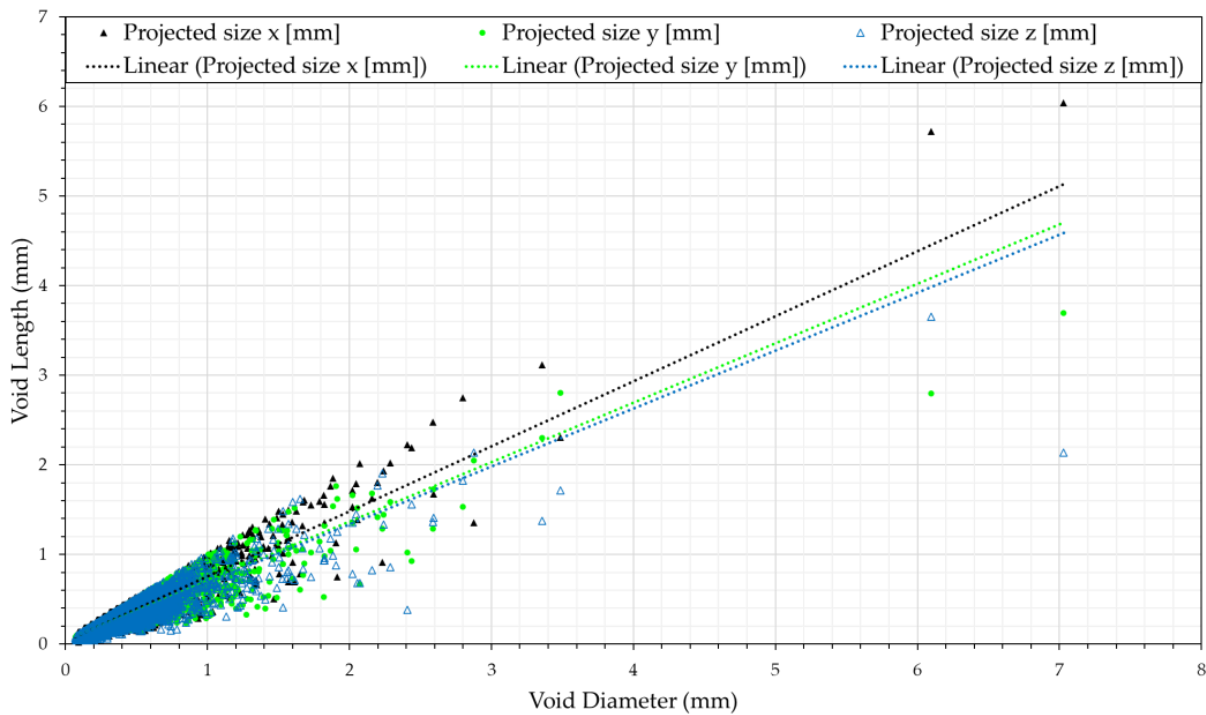


Figure 10. CAST-3DCP void topology from μ -CT scanning. The coefficients of determination (R^2) for x, y and z linear regression are 0.84, 0.85 and 0.83, respectively.

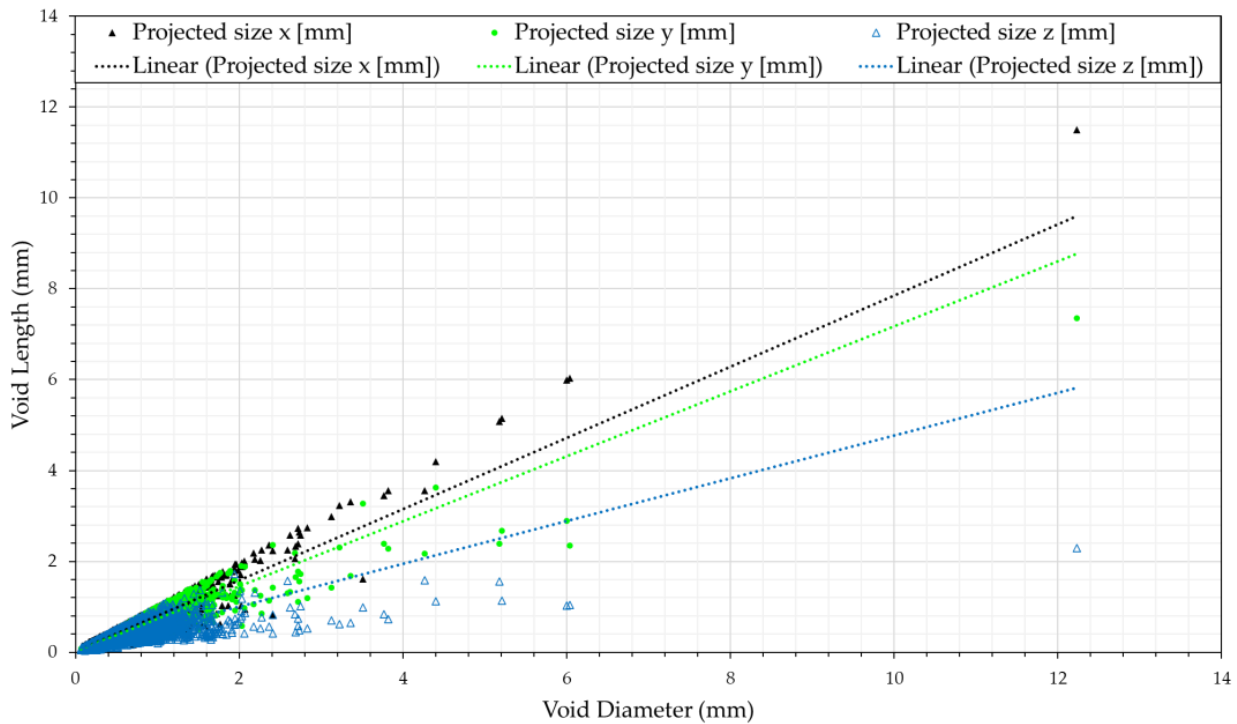


Figure 11. 3DCPOIB void topology from μ -CT scanning. The coefficients of determination (R^2) for x, y and z linear regression are 0.9, 0.89 and 0.74, respectively.

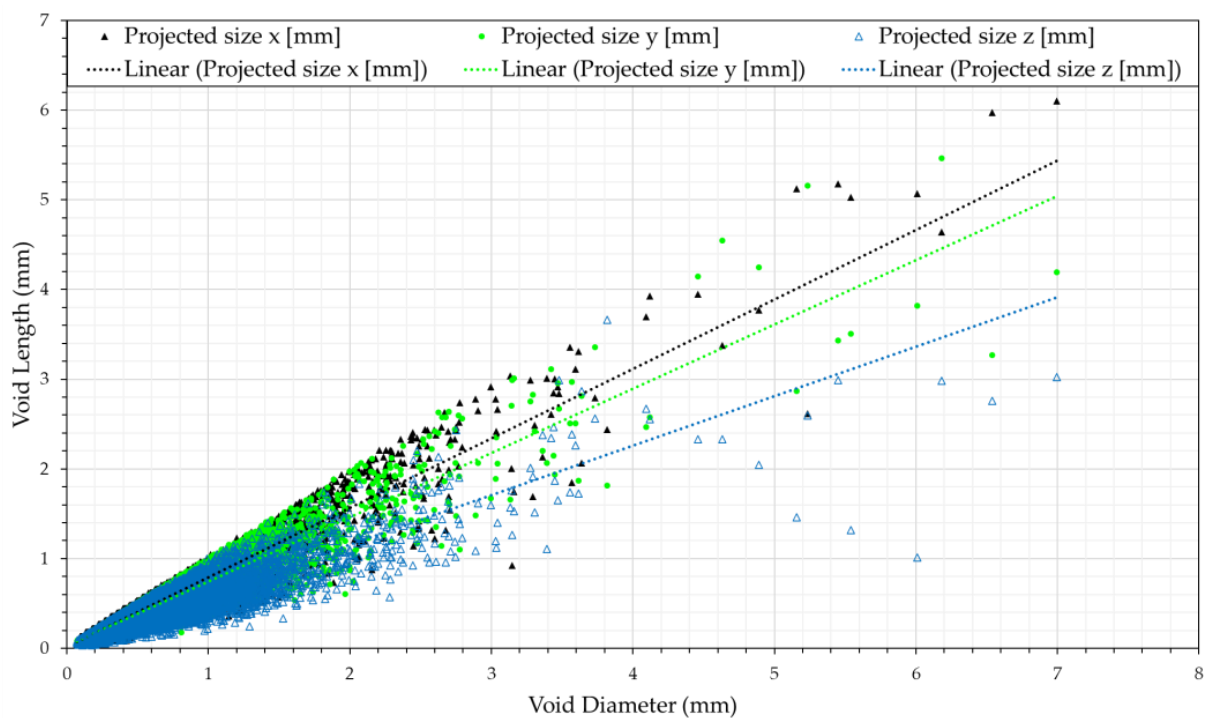
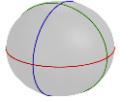

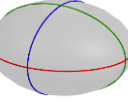
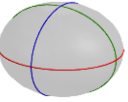


Figure 12. 3DCPOIT void topology from μ -CT scanning. The coefficients of determination (R^2) for x, y and z linear regression are 0.92, 0.91 and 0.86, respectively.

Table 6 gives a summary of the analysed data presented in Figures 9–12. It is evident from the normalised regression model gradients, as well as the normalised variances, that the CAST-CM specimen has the most spherical void topology. The CAST-3DCP specimen’s voids are slightly narrower than those of CAST-CM due to the pumping and extrusion

process. The 3D printed specimen's voids are considerably flatter due to the printing process, with the flattest voids present in the 3DCPOIB specimen. These results corroborate the findings presented in the previous section and confirm that oblate voids are present in this study's 3D printed specimens.

Table 6. Normalised 3D voids for each configuration based on their regression model gradients. Normalisation performed with respect to the x-direction (printing direction).

Specimen Configuration	Cartesian Direction	Regression Model Gradient	Normalised Gradient	Normalised Variance	Normalised 3D Void Graphic
CAST-CM	X	0.7835	1.00	0.007	
	Y	0.7876	1.01		
	Z	0.6931	0.88		
CAST-3DCP	X	0.7265	1.00	0.010	
	Y	0.6637	0.91		
	Z	0.6467	0.89		
3DCPOIB	X	0.7839	1.00	0.084	
	Y	0.7158	0.91		
	Z	0.4699	0.60		
3DCPOIT	X	0.7740	1.00	0.044	
	Y	0.7160	0.93		
	Z	0.5521	0.71		

4. Discussion

It is evident from the results that this study's hypothesis was evidenced to be correct. By analysing the μ -CT scanning data rigorously, it was demonstrated that the specimens tested for Poisson's ratio in this study do contain oblate voids, aligning with the printing direction, whereas the conventionally cast specimen contains mostly spherical voids, as deduced from Figures 9–12 and the summary in Table 6. The Poisson ratio for the conventionally cast concrete specimen was determined as 0.18, which is close to the lower bound of the typical Poisson ratio for cast concrete of 0.15, possibly ascribed to the total aggregate volume fraction of the mixture [6].

All the 3D printed specimens were found to have higher Poisson ratios than the cast specimen, confirming that adopting the Poisson ratio of conventionally cast concrete (even if the material is 3D printable and has been pumped and extruded) is inaccurate. Additionally, there is a directional dependency to the Poisson ratio of printed concrete; hence, it can be accepted as an anisotropic material property. In this study, specimens tested perpendicular to the printing direction (containing oblate voids, denoted OI) yielded a Poisson ratio of 0.21. Furthermore, specimens tested parallel to the printing direction (containing prolate voids, OIII) yielded a Poisson ratio of 0.24. This is the highest of all tested configurations, which is postulated to be due to the slender vertical concrete material located between the predominantly prolate voids experiencing increased lateral deformation under axial loading, similar to that of slender structural columns, but on a microscale. The opposite is also postulated to hold, i.e., the flat oblate voids in OI experience increased axial deformation under axial loading, due to the high tensile stress concentrations at the lateral sides of the flat voids, resulting in a lower Poisson ratio than that of OIII. This postulation can, at this stage, not be experimentally tested since μ -CT scanning is performed in a closed environment where a load cannot be applied to the specimen. The authors are uncertain at this stage why the Poisson ratio of the cast specimen is lower than both the 3D printed specimens when it would be expected to have a Poisson value between that of OI and OIII based on the fact that the voids in these specimens are predominantly spherical, i.e., between oblate and prolate. Interestingly, the OI and OIII

Poisson ratios do still fall within the typical Poisson ratio range for conventionally cast concrete of 0.15–0.25.

The OI and OIII Poisson values were found to be 17% and 33% higher than their cast equivalents in this study. Although only five specimens were tested per configuration, the ANOVA results indicate that there is a statistically significant difference between the means of the three configurations, as per Table 4, with a p -value an order of magnitude smaller than the significance value of 0.05. Based on the μ -CT scanning data analysis, where a significant difference in sphericity and compactness between CAST-3DCP and OI, OIII is observed in Figure 8, it can be deduced that the printing process, and not the pumping and extrusion process, primarily influences the void topology, and consequently the orthotropic nature of printed concrete. In the scenario where Poisson's ratio is required for analytical or computational modelling of 3D printed concrete elements, the authors recommend that representative tests, as conducted in this study, are performed to quantify the degree of orthotropy for inclusion in the modelling; adopting a single isotropic Poisson ratio may result in inaccuracies.

An interesting finding, though not explicitly investigated in this study but recommended for further research, is the spatial variation in total porosity and void topology of printed concrete, as per Table 5 and Figure 8. The sphericity and compactness values are lowest at the bottom of a printed structure and increase as a function of height. The bearing capacity of the fresh concrete may be inadequate to support the self-weight of successively deposited filament layers, resulting in large strains and increasingly oblate voids forming in the microstructure. Since it has been established that void topology is at the origin of the orthotropy, it could be postulated that the Poisson ratio may also vary spatially over the height of a printed object, both in the OI and OIII test directions. In the scenario where high stiffness develops rapidly in a deposited filament, as is the case in 2K printing systems where hydration is accelerated, the spatial variation in Poisson's ratio over the height of a printed element may reduce significantly.

5. Conclusions

This research set out to perform a preliminary investigation into the Poisson ratio of extrusion-based 3D printed concrete. Three-dimensionally printed specimens were prepared from an arbitrary printed element in two orthotropic directions: OI, denoting interlayers perpendicular to the testing direction, and OIII, denoting interlayers parallel to the testing direction. The specimens were equipped with target markers to accurately record lateral and longitudinal strains through digital image correlation technology. A reference case was also adopted and comprised conventionally cast specimens that were core-drilled from cast concrete cubes. Testing guidelines provided by ASTM C469-02 were followed to determine the Poisson ratios. Additionally, micro-computed tomography scans were performed on all specimens to investigate their microporosity, specifically the void topography. The main conclusions derived from the results of this study are:

1. Three-dimensionally printed concrete exhibits anisotropic behaviour. The Poisson ratios for the OI and OIII directions were 0.21 and 0.24, respectively;
2. Three-dimensionally printed concrete exhibits larger Poisson ratios than its cast counterpart. The same concrete mix that was 3D printed was also cast and tested, which yielded a Poisson ratio of 0.18. Although only five specimens were tested per configuration, a one-way ANOVA test confirmed that the means of the three groups are statistically different;
3. The μ -CT scanning results confirm the widespread presence of oblate voids in the 3D printed specimens of this study. For the OI direction, these voids are oblate with respect to the testing direction, whereas in the OIII direction, the voids are prolate. These varying void orientations are the cause of the observed anisotropy in printed concrete;
4. Results from the compactness and sphericity investigations indicate that the printing process has a larger influence on porosity topography than the pumping and

extrusion process. Hence, proper selection of printing parameters is paramount to reducing anisotropy;

5. A spatial variation in porosity and void topography was observed over the height of the 3D printed element. Although not explicitly tested in this research, it is postulated that the Poisson ratio might vary spatially over the height of a printed object.

This research forms a basis on which further, more detailed, investigations into the anisotropic behaviour of 3D printed concrete can be performed. The findings presented herein are especially valuable for modelling and designing 3D printed concrete structures, from the material to the structural level. Suggested focus points for future studies include (i) larger sampling, (ii) investigating potential spatiotemporal influence on Poisson's ratio and (iii) comparing anisotropy between various 3D concrete printing methods.

Author Contributions: Conceptualisation, J.K. and J.-P.v.d.W.; methodology, J.K. and J.-P.v.d.W.; software, J.-P.v.d.W.; validation, J.K. and J.-P.v.d.W.; formal analysis, J.-P.v.d.W.; investigation, J.-P.v.d.W.; resources, J.K.; data curation, J.-P.v.d.W.; writing—original draft preparation, J.K. and J.-P.v.d.W.; writing—review and editing, J.K.; visualisation, J.-P.v.d.W.; supervision, J.K.; project administration, J.K.; funding acquisition, J.K. All authors have read and agreed to the published version of the manuscript.

Funding: This research received no external funding.

Institutional Review Board Statement: Not applicable.

Informed Consent Statement: Not applicable.

Data Availability Statement: Not applicable.

Acknowledgments: The authors thank PPC Cement and Chryso SA for donating research material toward this study.

Conflicts of Interest: The authors declare no conflict of interest.

References

1. Hibbeler, R.C. *Mechanics of Materials*, 8th ed.; Fan, S.C., Ed.; Pearson Education: Singapore, 2011; ISBN 978-981-06-8509-6.
2. Evans, K.E. Auxetic Polymers: A New Range of Materials. *Endeavour* **1991**, *15*, 170–174. [\[CrossRef\]](#)
3. Xu, Y.; Zhang, H.; Schlangen, E.; Luković, M.; Šavija, B. Cementitious Cellular Composites with Auxetic Behavior. *Cem. Concr. Compos.* **2020**, *111*, 103624. [\[CrossRef\]](#)
4. Grant, R.J.; Lorenzo, M.; Smart, J. The Effect of Poisson's Ratio on Stress Concentrations. *J. Strain. Anal. Eng. Des.* **2007**, *42*, 95–104. [\[CrossRef\]](#)
5. Brauns, J.; Rocens, K. The Effect of Material Strength on the Behaviour of Concrete-Filled Steel Elements. *J. Civ. Eng. Manag.* **2004**, *10*, 177–182. [\[CrossRef\]](#)
6. Anson, M.; Newman, K. The Effect of Mix Proportions and Method of Testing on Poisson's Ratio for Mortars and Concretes. *Mag. Concr. Res.* **1966**, *18*, 115–130. [\[CrossRef\]](#)
7. Kruger, J.; du Plessis, A.; van Zijl, G. An Investigation into the Porosity of Extrusion-Based 3D Printed Concrete. *Addit. Manuf.* **2021**, *37*, 101740. [\[CrossRef\]](#)
8. van den Heever, M.; du Plessis, A.; Kruger, J.; van Zijl, G. Evaluating the Effects of Porosity on the Mechanical Properties of Extrusion-Based 3D Printed Concrete. *Cem. Concr. Res.* **2022**, *153*, 106695. [\[CrossRef\]](#)
9. Le, T.T.; Austin, S.A.; Lim, S.; Buswell, R.A.; Law, R.; Gibb, A.G.F.; Thorpe, T. Hardened Properties of High-Performance Printing Concrete. *Cem. Concr. Res.* **2012**, *42*, 558–566. [\[CrossRef\]](#)
10. Xiao, J.; Liu, H.; Ding, T. Finite Element Analysis on the Anisotropic Behavior of 3D Printed Concrete under Compression and Flexure. *Addit. Manuf.* **2021**, *39*, 101712. [\[CrossRef\]](#)
11. Wolfs, R.J.M.; Bos, F.P.; Salet, T.A.M. Hardened Properties of 3D Printed Concrete: The Influence of Process Parameters on Interlayer Adhesion. *Cem. Concr. Res.* **2019**, *119*, 132–140. [\[CrossRef\]](#)
12. Zhang, Y.; Zhang, Y.; She, W.; Yang, L.; Liu, G.; Yang, Y. Rheological and Harden Properties of the High-Thixotropy 3D Printing Concrete. *Constr. Build. Mater.* **2019**, *201*, 278–285. [\[CrossRef\]](#)
13. Nerella, V.N.; Hempel, S.; Mechtcherine, V. Effects of Layer-Interface Properties on Mechanical Performance of Concrete Elements Produced by Extrusion-Based 3D-Printing. *Constr. Build. Mater.* **2019**, *205*, 586–601. [\[CrossRef\]](#)
14. Mechtcherine, V.; Nerella, V.N.; Will, F.; Näther, M.; Otto, J.; Krause, M. Large-Scale Digital Concrete Construction—CONPrint3D Concept for on-Site, Monolithic 3D-Printing. *Autom. Constr.* **2019**, *107*, 102933. [\[CrossRef\]](#)

15. Mohan, M.K.; Rahul, A.V.; De Schutter, G.; Van Tittelboom, K. Extrusion-Based Concrete 3D Printing from a Material Perspective: A State-of-the-Art Review. *Cem. Concr. Compos.* **2021**, *115*, 103855. [[CrossRef](#)]
16. Davis, T.; Healy, D.; Bubeck, A.; Walker, R. Stress Concentrations around Voids in Three Dimensions: The Roots of Failure. *J. Struct. Geol.* **2017**, *102*, 193–207. [[CrossRef](#)]
17. van den Heever, M.; Bester, F.; Kruger, J.; van Zijl, G. Mechanical Characterisation for Numerical Simulation of Extrusion-Based 3D Concrete Printing. *J. Build. Eng.* **2021**, *44*, 102944. [[CrossRef](#)]
18. van den Heever, M.; Bester, F.; Kruger, J.; van Zijl, G. Numerical Modelling Strategies for Reinforced 3D Concrete Printed Elements. *Addit. Manuf.* **2022**, *50*, 102569. [[CrossRef](#)]
19. van den Heever, M.; Bester, F.; Pourbehi, M.; Kruger, J.; Cho, S.; van Zijl, G. Characterizing the Fissility of 3D Concrete Printed Elements via the Cohesive Zone Method. In *2nd RILEM International Conference on Concrete and Digital Fabrication*; Springer: Eindhoven, The Netherlands, 2020.
20. Bi, M.; Tran, P.; Xia, L.; Ma, G.; Xie, Y.M. Topology Optimization for 3D Concrete Printing with Various Manufacturing Constraints. *Addit. Manuf.* **2022**, *57*, 102982. [[CrossRef](#)]
21. Wu, Y.C.; Yang, Q.; Kong, X.; Zhi, P.; Xiao, J. Uncertainty Quantification for the Representative Volume Element of Geometrically Monoclinic 3D Printed Concrete. *Int. J. Solids Struct.* **2021**, *226–227*, 111102. [[CrossRef](#)]
22. Vantighem, G.; De Corte, W.; Shakour, E.; Amir, O. 3D Printing of a Post-Tensioned Concrete Girder Designed by Topology Optimization. *Autom. Constr.* **2020**, *112*, 103084. [[CrossRef](#)]
23. Valle-Pello, P.; Álvarez-Rabanal, F.P.; Alonso-Martínez, M.; del Coz Díaz, J.J. Numerical Study of the Interfaces of 3D-Printed Concrete Using Discrete Element Method. *Materwiss. Werksttech.* **2019**, *50*, 629–634. [[CrossRef](#)]
24. Wolfs, R.J.M.; Suiker, A.S.J. Structural Failure during Extrusion-Based 3D Printing Processes. *Int. J. Adv. Manuf. Technol.* **2019**, *104*, 565–584. [[CrossRef](#)]
25. Suiker, A.S.J. Mechanical Performance of Wall Structures in 3D Printing Processes: Theory, Design Tools and Experiments. *Int. J. Mech. Sci.* **2018**, *137*, 145–170. [[CrossRef](#)]
26. Nedjar, B. Incremental Viscoelasticity at Finite Strains for the Modelling of 3D Concrete Printing. *Comput. Mech.* **2022**, *69*, 233–243. [[CrossRef](#)]
27. Nguyen-Van, V.; Panda, B.; Zhang, G.; Nguyen-Xuan, H.; Tran, P. Digital Design Computing and Modelling for 3-D Concrete Printing. *Autom. Constr.* **2021**, *123*, 103529. [[CrossRef](#)]
28. Wolfs, R.J.M.; Bos, F.P.; Salet, T.A.M. Early Age Mechanical Behaviour of 3D Printed Concrete: Numerical Modelling and Experimental Testing. *Cem. Concr. Res.* **2018**, *106*, 103–116. [[CrossRef](#)]
29. Wolfs, R.J.M.; Bos, F.P.; Salet, T.A.M. Triaxial Compression Testing on Early Age Concrete for Numerical Analysis of 3D Concrete Printing. *Cem. Concr. Compos.* **2019**, *104*, 103344. [[CrossRef](#)]
30. Moini, R.; Olek, J.; Zavattieri, P.D.; Youngblood, J.P. Early-Age Buildability-Rheological Properties Relationship in Additively Manufactured Cement Paste Hollow Cylinders. *Cem. Concr. Compos.* **2022**, *131*, 104538. [[CrossRef](#)]
31. Ahmed, L. Dynamic Measurements for Determining Poisson's Ratio of Young Concrete. *Nord. Concr. Res.* **2018**, *58*, 95–106. [[CrossRef](#)]
32. Allos, A.E.; Martin, L.H. Factors affecting Poisson's ratio for concrete. *Build. Environ.* **1981**, *16*, 1–9. [[CrossRef](#)]
33. Wangler, T.; Pileggi, R.; Gürel, S.; Flatt, R.J. A Chemical Process Engineering Look at Digital Concrete Processes: Critical Step Design, Inline Mixing, and Scaleup. *Cem. Concr. Res.* **2022**, *155*, 106782. [[CrossRef](#)]
34. Kruger, J.; Zeranka, S.; van Zijl, G. A Rheology-Based Quasi-Static Shape Retention Model for Digitally Fabricated Concrete. *Constr. Build. Mater.* **2020**, *254*, 119241. [[CrossRef](#)]
35. Kruger, J.; van Zijl, G. A Compendious Review on Lack-of-Fusion in Digital Concrete Fabrication. *Addit. Manuf.* **2021**, *37*, 101654. [[CrossRef](#)]
36. ASTM C469; Standard Test Method for Static Modulus of Elasticity and Poisson's Ratio of Concrete in Compression. ASTM: West Conshohocken, PA, USA, 2002.
37. Kruger, J.; Van Den Heever, M.; Cho, S.; Zeranka, S.; van Zijl, G. High-Performance 3D Printable Concrete Enhanced with Nanomaterials. In *Proceedings of the International Conference on Sustainable Materials, Systems and Structures (SMSS 2019)*, Rovinj, Croatia, 20–22 March 2019; pp. 1–8.
38. Moelich, G.M. *Plastic Shrinkage Cracking and Other Evaporation-Related Impairments in 3D Printed and Cast Concrete*; Stellenbosch University: Stellenbosch, South Africa, 2021.
39. GOM GOM Correlate Pro. Available online: <https://www.gom.com/en/products/zeiss-quality-suite/gom-correlate-pro> (accessed on 18 January 2023).
40. Panda, B.; Mohamed, N.A.N.; Paul, S.C.; Singh, G.V.P.B.; Tan, M.J.; Šavija, B. The Effect of Material Fresh Properties and Process Parameters on Buildability and Interlayer Adhesion of 3D Printed Concrete. *Materials* **2019**, *12*, 2149. [[CrossRef](#)] [[PubMed](#)]

Disclaimer/Publisher's Note: The statements, opinions and data contained in all publications are solely those of the individual author(s) and contributor(s) and not of MDPI and/or the editor(s). MDPI and/or the editor(s) disclaim responsibility for any injury to people or property resulting from any ideas, methods, instructions or products referred to in the content.